

# Evaluating materials design parameters of hole-selective contacts for silicon heterojunction solar cells

Rachel Woods-Robinson<sup>\*</sup>, Angela N. Fioretti<sup>†</sup>, Jan Haschke<sup>‡‡</sup>, Mathieu Boccard<sup>†</sup>, Kristin A. Persson<sup>\*</sup>, and Christophe Ballif<sup>†</sup>

**Abstract**—Silicon heterojunction (SHJ) solar cell efficiencies are limited by parasitic absorption from the hydrogenated amorphous silicon (a-Si:H) front contact, but this may be mitigated by selecting an alternative carrier selective contact material with a wider band gap. When choosing such a material as the hole-selective contact (“p-layer”), alignment of the material’s valence band edge energy ( $E_{VB}$ ) with that of crystalline silicon (c-Si) is an important criterion, but several other material parameters can also influence band bending at the contact interface. Here, we simulate an (n)c-Si/(i)a-Si:H/p-layer interface to explore the influence of six materials parameters in a variable p-layer on SHJ performance. We find a strong influence on fill factor from thickness, doping, and  $E_{VB}$ , and on  $V_{OC}$  from interfacial defect density; notably, optimal  $E_{VB}$  is  $\sim 0.1$  eV higher than the valence band edge energy of a-Si:H. Multi-parameter sensitivity analyses demonstrate how performance is simultaneously influenced by  $E_{VB}$  and doping; thus, both parameters should be optimized alongside one another. To assess the influence of these parameters experimentally, we grow p-type  $\text{NiO}_x$  as a test-case p-layer, showing that fill factors decrease with oxygen content likely from increased misalignment of  $E_{VB}$ . Although modest efficiencies are achieved experimentally ( $>7\%$ ), what is important is that our model simulates performance trends. With these results, we apply a materials discovery pipeline to suggest new materials (e.g.  $\text{ZnTe}$ ,  $\text{BeTe}$ ) to try as p-layers in SHJ. This combination of simulations, experiments, and materials discovery informs a better understanding of contact selection in SHJ cells.

**Index Terms**—silicon heterojunction solar cells, carrier selective contacts, transparent conducting materials, materials design

## I. INTRODUCTION

Classical, two-side contacted silicon heterojunction (SHJ) solar cells currently lag behind the power conversion efficiency of homojunctions and all-back contacted architectures due to parasitic absorption of short-wavelength light.[1, 2] In SHJ devices using an n-type wafer and the hole-selective contact stack on the front-side, these challenges stem largely from this front contact stack, in which the typical requirements for an optimal contact stack—to be passivating, conductive, and carrier-selective[3]—are extended to include broadband transparency. Despite research efforts to develop an alternative p-type contact with improved transparency and carrier transport compared to standard p-doped amorphous silicon (p) a-Si:H,

<sup>\*</sup> University of California and Lawrence Berkeley National Laboratory, Berkeley, CA, 94720 USA

<sup>†</sup> Photovoltaics and Thin Film Electronics Laboratory, Institute of Micro-engineering, École Polytechnique Fédérale de Lausanne (EPFL), Neuchâtel, Switzerland

<sup>‡</sup> now with REC Solar Pte. Ltd., 20 Tuas South Ave. 14, Singapore 637312, Singapore

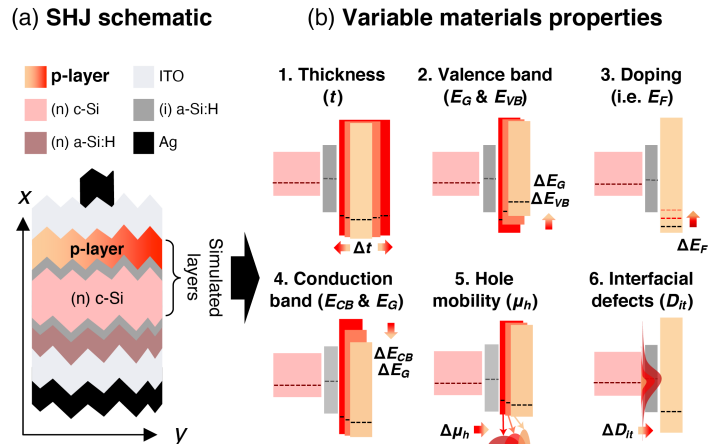


**Figure 1:** (a) Silicon heterojunction (SHJ) solar cell device schematic. The p-layer is the hole-selective contact, and is depicted with an orange-red color gradient to represent the variability of properties explored in this study. (b) Graphical schematic of the six variable materials parameters of the p-type semi-transparent hole-selective contact explored in this study. The three simulated layers are represented here: the pink rectangle is (n) c-Si, the grey rectangle is (i) a-Si:H, and the orange-red rectangles are the variable p-layer. The top and bottom edges of each rectangle are the conduction band edge and valence band edge, respectively, the dashed lines are the Fermi energies of each material, and the thick arrows represent increasing property value in the three different variable p-layer scenarios. The increased curvatures in the mobility schematic represents valence band edge dispersion (i.e. lower effective mass), and the  $D_{it}$  schematic represents a Gaussian-like distribution of interfacial defects.

such as  $\text{MoO}_x$ [4, 5, 6] or doped microcrystalline silicon,[7, 8] no SHJ cell based on these alternative contact materials has yet reached short circuit current densities ( $J_{SC}$ ) or front-surface transparencies of the best front-homojunction designs. One material challenge is that a high-performing material that is both p-type conducting and transparent across the visible spectrum has not yet been discovered.[9, 10, 11, 12]

In recent years, computational materials design based on screening databases of electronic structure calculations has given rise to the ability to identify new compounds with desirable properties for specific optoelectronic applications.[16] Some of these screening efforts have resulted in publications listing novel p-type transparent materials that remain mostly unexplored in experimental literature.[17, 18, 19, 20] These materials represent an untapped resource of possible candidates for p-type carrier-selective contact applications; a situation that is largely due to the absence of a strong link between SHJ technology and computational materials design. Such a link can be made for any given application by defining which material

**Table I:** AFORS-HET simulation parameters for each modeled layer.

Layer	(n) c-Si	(i) a-Si:H	Variable p-layer	Standard (p) NiO <sub>x</sub> *	Defect layer†
Thickness, $t$	180 $\mu\text{m}$	5 nm	0.1 – 300 nm	10 nm	1 nm
Band gap, $E_G$ (eV)	1.124	1.72	1 – 4.5	3.2	1.124
CB edge energy, $E_{CB}$ (eV)	4.05	3.9	1.5 – 2.75	1.8	4.05
VB edge energy, $E_{VB}$ (eV)	5.17	5.62	5.1 – 5.9	5	5.17
Electron doping, $N_D$ ( $\text{cm}^{-3}$ )	$1.56 \times 10^{15}$	1000	0	0	$1.56 \times 10^{15}$
Hole doping, $N_A$ ( $\text{cm}^{-3}$ )	0	0	$1 \times 10^{10} - 1 \times 10^{19}$	$5 \times 10^{15}$	0
Electron mobility, $\mu_n$ ( $\text{cm}^2 \text{V}^{-1} \text{s}^{-1}$ )	1335	20	$3\mu_p$	0.326	1335
Hole mobility, $\mu_p$ ( $\text{cm}^2 \text{V}^{-1} \text{s}^{-1}$ )	462.7	5	$1 \times 10^{-3} - 1 \times 10^3$	0.141	462.7
CB effective DOS, $N_C$ ( $\text{cm}^{-3}$ )	$2.84 \times 10^{19}$	$1 \times 10^{21}$	$1 \times 10^{20}$	$1 \times 10^{20}$	$2.84 \times 10^{19}$
VB effective DOS, $N_V$ ( $\text{cm}^{-3}$ )	$2.68 \times 10^{19}$	$1 \times 10^{21}$	$1 \times 10^{20}$	$1 \times 10^{20}$	$2.68 \times 10^{19}$
Dielectric constant, $dk$ (-)	11.9	11.9	11.75	11.75	11.9
Defects ( $\text{cm}^{-2} \text{eV}^{-1}$ )	single defect at $\frac{1}{2} E_G$	CB/VB tail, Gaussian A/D‡	—	—	continuous A/D‡: $10^7 - 10^{17}$

\*“Standard” values for a low p-type doped NiO<sub>x</sub>. [13, 14, 15] †Interfacial defect layer modeled between (n) c-Si and (i) a-Si:H to simulate  $D_{it}$ . ‡“A/D” = acceptor and donor defects.

properties are most critical and determining their relevant ranges using targeted numerical simulations. The results can then be used to select candidate materials from the existing literature via computational screening.

In this work, we use 1D numerical solar cell simulations to explore the impact of relevant hole-selective contact (i.e. “p-layer”) material properties on the performance of a two-side contacted SHJ solar cell, as depicted in **Figure 1(a)**. These simulations allow systematic tuning of one variable at a time or multiple variables simultaneously, as shown schematically in **Figure 1(b)** with the orange-red color gradient, over a wide range that would otherwise be inaccessible experimentally. This approach allows us to assess the importance of each material parameter to the final solar cell performance and to elucidate the limits beyond which power conversion efficiency decreases. Previous literature has assumed valence band (VB) edge alignment to crystalline silicon (c-Si) as a principle design parameter, so we select nickel oxide (NiO<sub>x</sub>, with a VB edge energy  $E_{VB, NiO_x}$  close to that of c-Si,  $E_{VB, c-Si}$ ) as a test hole-selective contact material for both simulations and experiments in a full device stack. NiO<sub>x</sub> has only rarely been studied as a hole-selective contact in SHJ solar cells. [21, 22] There are only a few reports of solar cell performance, and highest reported efficiencies up to 12.4% and open circuit voltage ( $V_{OC}$ ) values up to 510 mV. [22] Most notably, its tunable VB edge energy and facile growth conditions make it a suitable test material. The resulting insights are then used to guide new materials selection criteria, assess the tolerances of such criteria, and propose a list of as-yet underexplored materials suitable for application as hole-selective contacts in the SHJ architecture.

## II. METHODOLOGY

### A. Simulations and calculations

Device modeling was performed using the AFORS-HET (Automat FOR Simulation of HETerostuctures) v2.5 1D numerical simulation software. [23, 24] As depicted in the cell schematic in **Figure 1(a)**, we modeled the cell as a three-layer structure consisting of n-type crystalline silicon “(n) c-Si,” intrinsic hydrogenated amorphous silicon “(i) a-Si:H,” and the variable p-type hole-selective contact “p-layer.” We assumed

the other layers to be optimized, so excluded them and added flat-band Schottky interfaces at each side of the device stack.

**Table I** reports the simulation parameters of each layer. Values for (n) c-Si and (i) a-Si:H are based on AFORS-HET standard layers. [25, 26, 27, 28] and “Standard (p) NiO<sub>x</sub>” values are from the literature for a thin film with low hole doping (note that hole doping density can be much higher and many of these values are tunable, as we discuss subsequently). [13, 14, 15] NiO<sub>x</sub> is a test-case for the variable p-layer, and the variable p-layer parameters were varied as depicted graphically in **Figure 1(b)**—namely thickness, VB edge energy  $E_{VB}$  (i.e. negative ionization energy; we will define  $E_{VB}$  as a positive value herein), band gap  $E_G$ , hole doping concentration  $N_A$  (i.e. acceptor density, which determines the position of the Fermi level,  $E_F$ ), hole mobility  $\mu_p$ , and interfacial defect density  $D_{it}$ —within the range as reported in column “Variable p-layer.” During variation of a single parameter, “Standard (p) NiO<sub>x</sub>” values were used for all other parameters (except for  $E_{VB}$ , as discussed subsequently).

Effective interfacial defect density  $D_{it}$  was simulated using a common method from the literature. [29, 30] adding a thin 1 nm defective layer in between the (n) c-Si and (i) a-Si:H layers. This layer is a proxy for any interfacial defects that could occur between the modeled layers. As described in the “Defect layer” column of **Table I**, this layer has properties similar to c-Si, with continuous defects across the c-Si band gap. These defects were modeled as continuous donor-like (D) and acceptor-like (A) in the upper and lower halves of the band gap, respectively, and  $D_{it}$  was varied between  $10^7 - 10^{17} \text{ cm}^{-2} \text{eV}^{-1}$ . Electron and hole capture cross-sections were set to  $10^{-14} \text{ cm}^2$ , as is conventional in AFORS-HET simulations investigating  $D_{it}$  in various materials. [29, 31] Optical parameters in the AFORS-HET model were set to n and k values for silicon; we performed an uncertainty analysis using ellipsometry derived optical parameters for NiO<sub>x</sub> thin films. [16] and observed no change in performance.

For *ab initio* materials modeling of different compositions of NiO<sub>x</sub>, NiO (mp-19009) and NiO<sub>2</sub> (mp-35925 and mp-25428) were selected from the Materials Project (MP) database as the end-point compounds of NiO<sub>x</sub> ( $1 < x < 2$ ). NiO is the rocksalt structure, with octahedral coordination of both Ni and

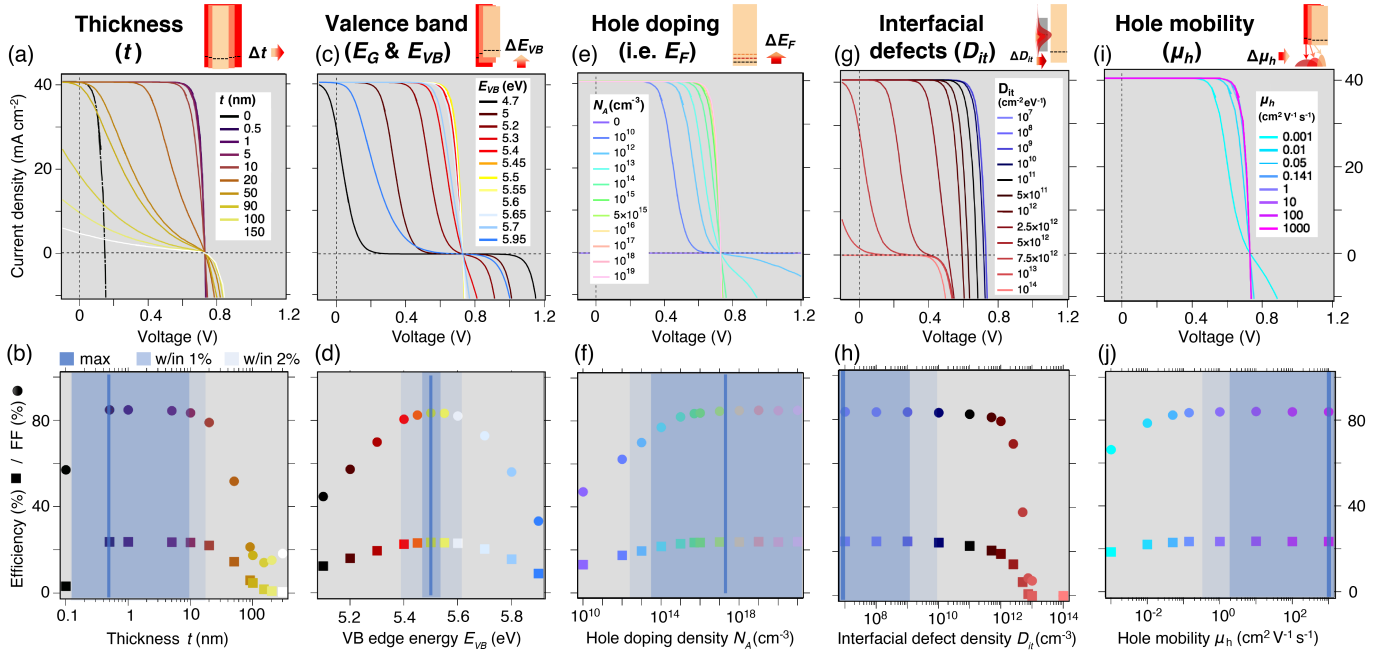


**Figure 2:** Simulated JV curves (top row) and plotted solar cell characteristics (bottom row) for the variations of five material parameters depicted in Figure 1: thickness (a–b), valence band edge energy (c–d), hole doping (e–f), hole mobility (g–h), and interfacial defect density (i–j). Blue shaded regions in the bottom row indicate regions where fill factor is within 1% and 2% of the maximum computed value.

O. NiO<sub>2</sub> (mp-35925) is a layered compound with octahedrally coordinated Ni atoms (while mp-25428 is a computationally predicted distorted derivative of the NiO rocksalt structure). Structures were relaxed using density functional theory (DFT), with the projector augmented wavefunction (PAW) method[32, 33] as implemented in the Vienna *Ab Initio* Simulation Package (VASP),[34, 35] within the Perdew-Berke-Ernzerhof (PBE) Generalized Gradient Approximation (GGA),[36] and standard MP calculation parameters.[37] Branch point energy (BPE) calculations—which effectively average the CB and VB dispersion in a given material’s computed band structure, assign an energy value based on this calculation, and then align this energy to that of another material to compare band edges—were used as a qualitative computational proxy for band alignment.[38] The branch point energy (BPE) of NiO and NiO<sub>2</sub> were calculated using the Matminer (Materials Data Mining) simulation package,[39] four VBs and two CBs were considered for the BPE calculation, and a sensitivity analysis was performed on various band consideration scenarios as outlined in the literature.[16]

### B. Solar cell fabrication and characterization

Solar cells were fabricated on 195  $\mu\text{m}$  thick, textured, n-type float zone wafers with a resistivity of 2–3  $\Omega\text{cm}$ . Plasma-enhanced chemical vapor deposition (PECVD) was used to deposit  $\sim 9$  nm of hydrogenated intrinsic amorphous silicon (a-Si:H) on the front and back sides, followed by  $\sim 30$  nm of n-type doped a-Si:H as the electron-selective contact on the back. NiO<sub>x</sub> layers were sputter-deposited on the front to a uniform thicknesses of approximately 10 nm, 20 nm, and 50 nm. All reported thicknesses were measured on flat glass by ellipsometry for the Si layers or by stylus profilometry for the NiO<sub>x</sub> layers. Sputter deposition was carried out at a substrate

temperature of 60 °C with a working pressure of 1.70  $\mu\text{bar}$  using a 4-inch ceramic NiO target in a chamber with  $\sim 3\text{--}5 \times 10^{-7}$  mbar base pressure. Oxygen was supplied to the chamber as a mixture of 5% O<sub>2</sub> in Ar at flow rates of  $\sim 0\text{--}9$  sccm (corresponding to 0–4.5% O<sub>2</sub>; we will use flow rate values herein) with the balance required to maintain working pressure made up by pure Ar and a constant total flow rate. After NiO<sub>x</sub> deposition, cells were finished by sputtering tin-doped indium oxide (ITO) followed by silver full area on the back and through shadow masks on the front to define three  $\sim 1 \times 1$  cm cells per quarter wafer. Cells were then annealed in air for 20 minutes at 210°C. Current-voltage characteristics (JV) were collected on finished cells using a Wacom Electric Co. Super Solar Simulator with AM 1.5G illumination and Keithley sourcemeters.

## III. RESULTS AND DISCUSSION

### A. Simulated sensitivity of materials parameters

Using AFORS-HET, we simulate solar cell performance for the various scenarios depicted in Figure 1. Unless a given parameter is being varied, the default values of the p-layer are assigned to those of “Standard (p) NiO<sub>x</sub>” in Table I — namely  $t = 10$  nm,  $N_A = 5 \times 10^{15}$  cm<sup>-3</sup>,  $\mu_p = 0.151$  cm<sup>2</sup>V<sup>-1</sup>s<sup>-1</sup> — with the exception of  $E_{VB}$ , which is assigned to the optimal value of 5.5 eV as discussed subsequently. Note that the low doping and low mobility are intended to be representative of a weakly p-type and poorly ordered material, as is expected to be the case for the envisioned new materials.

1) *Single-parameter sensitivity analysis:* To first illustrate our single-parameter sensitivity analyses, we simulate the influence of thickness on solar cell properties, and plot results in **Figure 2(a)** and (b). Simulated JV curves are shown in panel (a) and tracked fill factor (FF) and efficiencies ( $\eta$ ) are shown

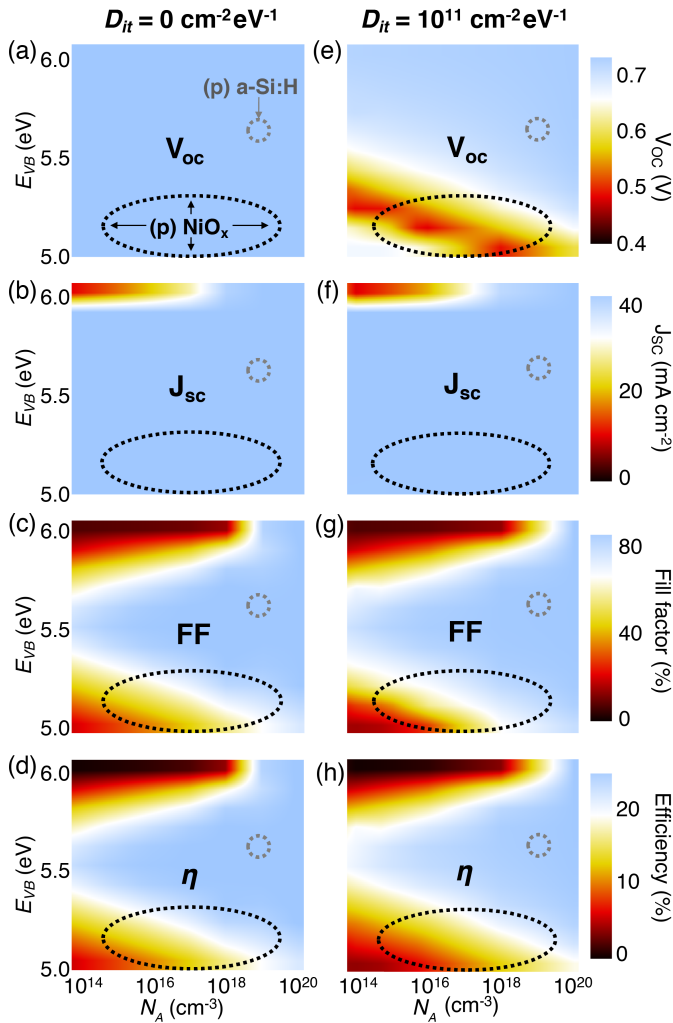


**Figure 3:** Heat maps depicting the simultaneous influence of doping and valence band edge energy on simulated SHJ solar cell properties (a) open circuit voltage, (b) short circuit current density  $J_{SC}$ , (c) fill factor FF and (d) efficiency  $\eta$  for a p-layer with no interfacial defect densities. (e), (f), (g), and (h) plot the same heat maps, respectively, but include interfacial defect densities of  $10^{11} \text{ cm}^{-2} \text{ eV}^{-1}$ . The dotted ovals indicate approximate ranges of  $E_{VB}$  and hole doping density reported in the literature for (p)  $\text{NiO}_x$  (black) and (p) a-Si:H (grey).

in panel (b), with blue shading indicating ranges of highest cell efficiency. We find that the thinnest p-layers ( $\sim 10$  nm or less) lead to highest performances, with maximum efficiencies and FF of  $\sim 23.8\%$  and  $\sim 84.8\%$ , respectively. Above 10 nm, an S-shaped JV curve is observed, leading to a significant drop in efficiency and FF.  $V_{OC}$  remains constant, but  $J_{SC}$  begins to decrease for thicknesses greater than  $\sim 90$  nm until efficiency is effectively zero at 200 nm. We note that this simulation does not include tunneling effects. Thickness is an extrinsic parameter and can be varied during growth for any given material; we will focus more on intrinsic materials parameters herein to align with our materials discovery approach.

Second, we assess the influence of valence band edge energy  $E_{VB}$  on simulated solar cell properties, and plot results in Figure 2(c) and (d). By varying  $E_{VB}$  with other parameters constant, we observe optimal solar cell performance at  $E_{VB}$  of 5.5 eV, correlating to an electron affinity of 2.3 eV with a gap of 3.2 eV. For a hole doping density of  $5 \times 10^{15} \text{ cm}^{-3}$ , highest

efficiencies and FF are  $\sim 24.8\%$  and  $\sim 84.4\%$ , respectively. The fill factor and efficiency remain at 2% of the optimal value for VB edge offsets (referring here to the offset from the optimum, not the offset with  $E_{VB,c-Si}$  or  $E_{VB,a-Si:H}$ ) of  $\pm 0.1$  eV, and then drop relatively symmetrically on either side. At the optimal  $E_{VB}$  alignment the JV curves appear ideal, while an S-shape onset occurs at misaligned  $E_{VB}$  values. These curves all appear to have the same  $J_{SC}$  and  $V_{OC}$ , though in the misaligned cases the JV curve flattens out at lower voltages. Importantly, the optimal  $E_{VB}$  does *not* occur at  $E_{VB,c-Si}$  (5.16 eV), as we had initially hypothesized since the (i) a-Si:H layer is so thin. Rather, it is closer to  $E_{VB,a-Si:H}$  (5.62 eV), but in fact at a slightly lower energy of 5.5 eV (closer to vacuum). This may indicate that the desired p-layer  $E_{VB}$  alignment for optimal performance is to the *quasi-Fermi energy* of holes ( $E_{F,p}$ ) at the (i) a-Si:H / p-layer interface under illumination and standard operating conditions, rather than simply to  $E_{VB,a-Si:H}$ .

Next, Figure 2(e) and (f) demonstrate that solar cell performance increases with higher hole doping in the p-layer, as expected, but only up to a certain threshold doping. For an  $E_{VB}$  of 5.5 eV, so long as doping is greater than approximately  $10^{16} \text{ cm}^{-3}$  FF and  $\eta$  only negligibly improve. Below  $10^{15} \text{ cm}^{-3}$  the FF decreases according to simulations, and we would expect  $V_{OC}$  to decrease in an experimental device where defects are included as in (g) (see next section). This suggests that in the SHJ device configuration explored in this paper, hole doping does not have to be as high as initially expected, so long as the  $E_{VB}$  is within  $5.5 \pm 0.1$  eV and passivation is sufficient.

Using the defect-layer approach outlined in the Methodology section, we fix other parameters and vary interfacial defect density  $D_{it}$ . We find in Figure 2(g) and (h) that solar cell performance remains unchanged to  $D_{it}$  values up to  $\sim 10^8 \text{ cm}^{-2} \text{ eV}^{-1}$ , after which the  $V_{OC}$  begins to drop with increased  $D_{it}$ . At about  $10^{11} \text{ cm}^{-2} \text{ eV}^{-1}$ , efficiency has decreased by over 15%. At  $D_{it}$  values greater than  $\sim 2.5 \times 10^{12} \text{ cm}^{-2} \text{ eV}^{-1}$ , the fill factor starts to drop significantly, and efficiencies of cells with  $D_{it} > 10^{13} \text{ cm}^{-2} \text{ eV}^{-1}$  are effectively zero. These findings corroborate literature reports for  $\text{NiO}_x$  cells, where increasing  $D_{it}$  above  $\sim 2 \times 10^{10} \text{ cm}^{-2} \text{ eV}^{-1}$  led to a steep decline in efficiency,[21] though only one set of conditions was assessed. We acknowledge that it is actually a function of both the capture cross-section and  $D_{it}$  that influences recombination rates, and thus  $V_{OC}$ ,[40] though we refer only to  $D_{it}$  herein for simplicity. As with all these parameters discussed so far, only  $D_{it}$  was varied, omitting important cross-interactions. To get the full picture, it is important to assess the influence of each parameter on one another and this will be done in subsection ‘‘Multi-parameter sensitivity analysis.’’

Panels (i) and (j) demonstrate that hole mobility ( $\mu_h$ ) is less important than the other parameters discussed so far. In this case we hold the ratio between hole and electron mobility constant at 1:3, and vary hole mobility by six orders of magnitude. Similarly to  $N_A$ , increasing  $\mu_h$  does indeed increase performance, though less significantly than the other parameters and only up to a threshold. Anything greater than approximately  $0.1 \text{ cm}^2 \text{ V}^{-1} \text{ s}^{-1}$  yields only negligible improvements. This finding is favorable, since very few optically transparent materials with highly mobile holes exist in practice. However, we acknowledge

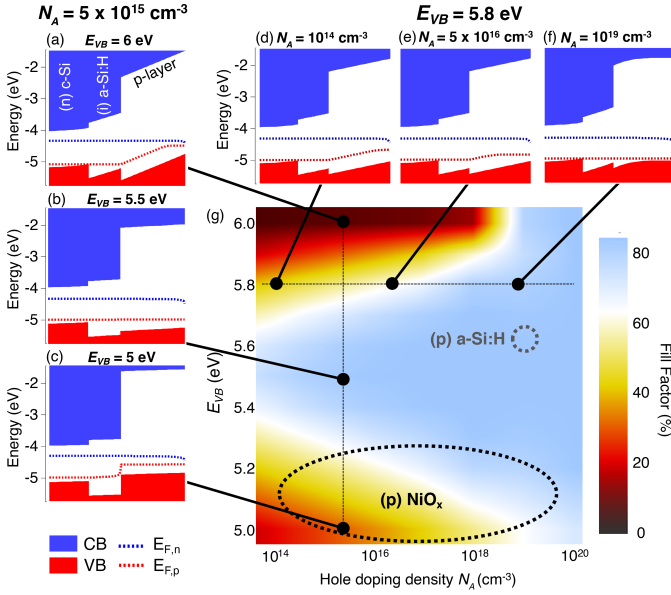


**Figure 4:** Band diagrams at maximum power point (mpp) for six different p-layer combinations of VB edge energy ( $E_{VB}$ ) and hole doping density ( $N_A$ ). The three diagrams on the left (a–c) are at constant  $N_A$  and varied  $E_{VB}$ , while the three upper diagrams (d–f) are at constant  $E_{VB}$  and varied  $N_A$ . As described in the legend (lower left corner), blue shadings are the conduction band states in the device (CB), dotted blue lines are the electron quasi-Fermi levels ( $E_{F,n}$ ), red shadings are the valence band states in the device (VB), and dotted red lines are the hole quasi-Fermi levels ( $E_{F,p}$ ). Black lines indicate the location of each condition studied on (g) the fill factor heat map from Figure 3(c). For reference, the positions of p-type  $\text{NiO}_x$  and p-type a-Si:H are plotted in (g) with their experimental  $E_{VB}$  alignments, 5.0 eV and 5.6 eV, respectively, and standard hole doping densities,  $5 \times 10^{14} \text{ cm}^{-3}$  and  $10^{20} \text{ cm}^{-3}$ , respectively.

this relies on the assumption that our choice of VB effective density of state (DOS)  $N_V$  ( $10^{20} \text{ cm}^{-3}$ ) is reasonable. We also find that independently varying the conduction band energy  $E_{CB}$  in this configuration has a negligible effect on the solar cell performance. Additionally changing  $E_G$  has a negligible impact in this model until  $E_G$  is less than that of c-Si (1.124 eV), though we note that band gaps in the visible range (less than  $\sim 3.1$  eV) can induce parasitic absorption in real devices which is not accounted for in this simulation. Thus, these findings are not reported in Figure 2.

2) *Multi-parameter sensitivity analysis:* In **Figure 3** we plot heat maps depicting multi-parameter variation of  $N_A$  and  $E_{VB}$  in the p-layer, for  $D_{it}$  values of 0 and  $10^{11} \text{ cm}^{-2}\text{eV}^{-1}$ , on the solar cell’s  $V_{OC}$ ,  $J_{SC}$ , FF and efficiency ( $\eta$ ). These simulations assume a p-layer thickness of 10 nm, and other “variable p-layer” parameters from Table I. The blue regions in panels (d) and (h) correspond to highest efficiencies, with white indicating a drop to below 20% efficiency. For cells with no  $D_{it}$  (a–d), regardless of doping, we observe the highest solar cell performance at  $E_{VB}$  values of 5.5 eV, corroborating optimal alignment from Figure 2. Figure 3(c) shows that the drops in efficiency stem nearly entirely from reductions in FF, where JV curves are S-shaped. Panel (b) shows  $J_{SC}$  remains relatively constant, except at  $E_{VB}$  values of 6 eV or greater and  $N_A$  below  $10^{18} \text{ cm}^{-3}$ , while (a) shows  $V_{OC}$  remains constant in this simulation space. Notably, we observe a window of high performance that is narrow at low  $N_A$  and widens at higher  $N_A$ . This suggests that p-layers with high hole doping are more

tolerant to misalignments in VB edge position, while those with low  $N_A$  only perform well if their  $E_{VB}$  is nearly exactly 5.5 eV. Both positive and negative misalignments lead to reduced performance, though too-high  $E_{VB}$  values drop off even steeper than too-low values due to an additional drop in  $J_{SC}$ , and we will investigate the physical reasons for these trends subsequently.

Figure 3(e–h) depicts simulated cells with all the same conditions except for an increased  $D_{it}$  of  $10^{11} \text{ cm}^{-2}\text{eV}^{-1}$ , demonstrating the interplay of three materials parameters from Figure 1. The biggest distinction is shown in panel (e): the reduction in  $V_{OC}$  for lower values of  $E_{VB}$ , likely trending with  $E_F$ . This influences efficiency at lower values of  $E_{VB}$ . We observe that at a given hole doping, the window of high efficiency reduces somewhat at elevated  $D_{it}$ , indicated by the shrinking of the blue region in panel (h). However, so long as optimal alignment and high doping are retained, high performance is still achievable despite interfacial defects, which is promising for practical applications. Additionally, optimal efficiency is not constant at 5.5 eV as in panel (d), but rather it is shifted somewhat towards higher  $E_{VB}$  as  $N_A$  increases; at hole dopings of  $10^{20} \text{ cm}^{-3}$ , efficiency is highest at  $E_{VB}$  values of 5.8–5.9 eV (24.86%) rather than 5.5 eV (24.78%), though differences are quite low. This is due to the trade-off between the increase of  $V_{OC}$  and decrease of FF with  $E_{VB}$ , as depicted in panels (e) and (g). We note that in the AFORS-HET simulations,  $V_{OC}$  is not affected in the absence of defects (a) since no current is extracted; however, since defects are virtually unavoidable in real devices,  $V_{OC}$  is expected to be impacted even with low defect densities (e).

In all graphs of Figure 3, the black dotted ovals indicate the range of likely  $E_{VB}$  and  $N_A$  in  $\text{NiO}_x$ , according to reported values in the literature.[41, 42, 43] Without including detrimental  $D_{it}$ , it appears that standard (p)  $\text{NiO}_x$  with  $N_A$  of  $5 \times 10^{16} \text{ cm}^{-3}$  and an  $E_{VB}$  at 5.0 eV is likely *not* an ideal candidate as a hole-selective contact, since FF and  $\eta$  drop to 27.6% and 8.1%. This only gets worse with high  $D_{it}$ , as  $V_{OC}$  and FF drop significantly to  $\sim 24\%$  and 644 mV, leading to efficiencies of  $\sim 6.3\%$ . However, significant engineering advances in electronic properties to lower the valence band edge (increase  $E_{VB}$ ) while maintaining high doping and low  $D_{it}$  could push performance higher into the blue region. This compares with (p) a-Si:H (grey dotted circles) doped to approximately  $10^{19} \text{ cm}^{-3}$ ,[44] with a combined doping and alignment leading to high electronic performance and efficiencies of 25.4%, regardless of  $D_{it}$ . Since (p) a-Si:H has ideal  $N_A$  and  $E_{VB}$ , these contacts have a higher  $D_{it}$  tolerance than  $\text{NiO}_x$ .

3) *Band alignments to understand performance trends, and discussion of quasi-Fermi levels:* To illustrate how and why the materials properties discussed above influence solar cell performance, we plot simulated band alignment diagrams at various conditions in **Figure 4**. In panel (g) we use the fill factor heatmap from Figure 3(c) to guide our location in parameter space, with the vertical thin dotted line indicating constant hole doping and the horizontal thin dotted line indicating constant VB edge energy. Filled black circles indicate the specific conditions investigated. For each circle, band diagrams are plotted under illumination at maximum power point (mpp), where blue shadings are the conduction band states in the

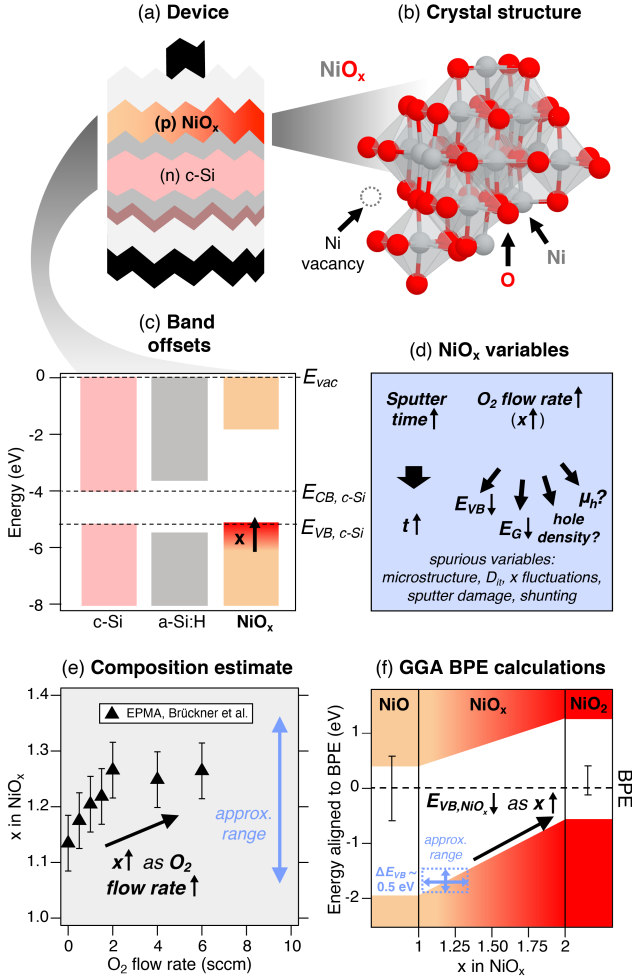


**Figure 5:** (a) Device schematic with  $\text{NiO}_x$  as the p-type hole-selective contact, with a red gradient indicating variable properties in this study. (b) Crystal structure of a representative  $\text{NiO}_x$  compound ( $\text{Ni}_5\text{O}_6$ , mp-754806), where Ni vacancies lead to p-type conductivity and local distortions.[45] (c) Band offset schematic of the three simulated layers, comparing  $\text{NiO}_x$  to n-Si and a-Si:H. Dotted lines correspond to the band edges of c-Si and the vacuum energy  $E_{vac}$ . The red gradient and “x” label illustrates that the VB edge energy moves closer to  $E_{vac}$  as x increases. (d) Extrinsic parameters targeted in our experiments, and their influence on intrinsic parameters. (e) Approximate x values for given  $\text{O}_2$  flow rate, with literature values from Brückner et al.[46] (f) Band positions of rocksalt NiO and layered  $\text{NiO}_2$  calculated using a GGA functional and aligned to branch point energy (BPE) values. Note that this is a *qualitative* alignment, and the y axis energies are not equivalent to the *quantitative* alignment energies in (c). For  $\text{NiO}_x$  compounds between these two end-points, we plot a linear relation assuming commensurate structures and no bowing. Thus, we would expect the VB edge to shift towards vacuum as x increases.

device (CB), dotted blue lines are the electron quasi-Fermi levels ( $E_{F,n}$ ), red shadings are the valence band states in the device (VB), and dotted red lines are the hole quasi-Fermi levels ( $E_{F,p}$ ). The (n) c-Si layer is the left-most layer, the (i) a-Si:H is the center layer, and the variable p-layer is the right-most layer, as shown in panel (a).

First, we observe changes in band alignments at a constant hole doping of  $5 \times 10^{15} \text{ cm}^{-3}$  in Figure 4(a–c). At the well-aligned  $E_{VB}$  value of 5.5 eV depicted in (b), the position of  $E_{F,p}$  is preserved throughout the p-layer at the same energy level as in the c-Si layer. This is the signature of a high-performing hole contact.[47] At misaligned  $E_{VB}$  values of 6.0 eV (a), however,

the p-layer is depleted due to the band offset, and band edges thus bend upwards sharply. Under illumination,  $E_{F,p}$  also bends upwards due to the resistivity of this depleted layer, and nearly meets the  $E_{F,n}$  over the thickness of the p-layer. This results in a loss of quasi-Fermi level (QFL) splitting—the difference between the electron quasi-Fermi level ( $E_{F,n}$ ) and hole quasi-Fermi level ( $E_{F,p}$ )—inside the contact itself. Thus, we would expect thinner layers or layers of higher mobility to perform better at this condition. Finally, at misaligned  $E_{VB}$  values of 5.0 eV depicted in (c), QFL splitting is lost immediately at the onset of the p-layer due to the sharp positive VB edge offset. This is the case that correlates approximately with standard  $\text{NiO}_x$ . Here,  $E_{F,p}$  in the p-layer is too low (around 4.5 eV), leading to a hole depletion along the (i) a-Si:H layer which causes the drop in  $E_{F,p}$  at the (i) a-Si:H / p-layer interface upon charge extraction.

Second, in Figure 4(d–f) we observe changes in band alignments at a constant  $E_{VB}$  of 5.8 eV, where a negative band offset leads to similar upward  $E_{F,p}$  bending. At low hole doping values of  $10^{14} \text{ cm}^{-3}$  in panel (d), the situation is similar to case (a) with  $E_{F,p}$  decreasing through the contact due to the resistance in the depleted p-layer. As doping increases in (e), a flat  $E_{F,p}$  can be maintained in part of the contact thickness due to the larger hole reservoir in this higher doped layer, enabling a higher conductivity to hole extraction in this illuminated device scenario. This allows for a larger QFL splitting to be maintained, mitigating the S-shape and improving FF. At  $N_A$  densities of  $10^{19} \text{ cm}^{-3}$  (f), high doping leads to a narrow depleted thickness in the p-layer, ensuring high conductivity of the p-layer throughout its thickness (including within the depletion zone). Importantly, in these iso- $E_{VB}$  simulations, the work function  $E_F$  increases with doping, also influencing the band bending. This is similar to the formation of an Ohmic contact between a highly doped semiconductor and a metal. In such a situation, the  $E_{F,p}$  does not bend upwards at all and performance is optimal.

This assessment reveals the importance of the p-layer’s Fermi level in determining the performance of the entire SHJ cell, and highlights that high doping is key to enable non-ideally-aligned materials to still perform well as hole-selective contacts. This high doping is also key in ensuring a good contact with the eventual transparent electrode, making it a stringent feature for any novel p-type material.[48] As a concluding note for this simulation section, we emphasize that the results shown here are only guidelines for idealized systems, and that effects stemming from the influence of the transparent electrode or from Fermi level pinning were not accounted for. Additionally, only 1D effects were simulated, and the rudimentary optical model used in AFORS-HET may be oversimplifying optical effects. Accurately reproducing these phenomena lie beyond the scope of this simulation software, yet is a crucial part of real-world solar cells.

### B. Case study: sputtered p-type $\text{NiO}_x$ as a hole-selective contact

To illustrate the influence of various p-layer parameters from Figure 1 on solar cell properties, we fabricate SHJ devices using sputtered p-type  $\text{NiO}_x$  as a test-case variable

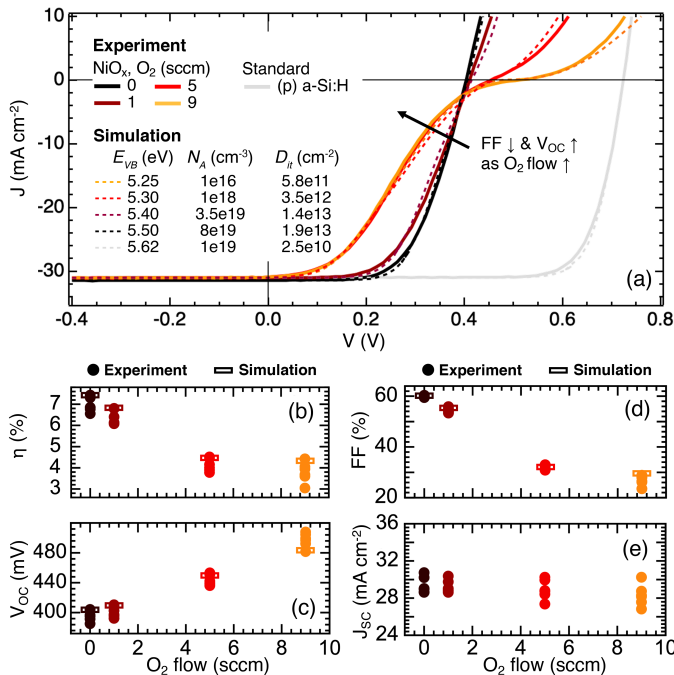


**Figure 6:** (a) JV curves for  $NiO_x$ -contacted silicon heterojunction solar cells (solid lines), with oxygen flow rates in the  $NiO_x$  layer of 0, 1, 5 sccm, and 9 sccm, and for a standard cell with a (p) a-Si:H contact. Fits for the simulations used in this study are shown with dashed lines, with simulated parameters reported in the legend. Statistical analysis of these cells for solar cell performance parameters (b) efficiency ( $\eta$ ), (c) fill factor (FF), (d)  $V_{OC}$ , and (e)  $J_{SC}$

p-layer, as depicted in **Figure 5(a)**. A representative crystal structure of  $NiO_x$  is shown in **Figure 5(b)** (in this case, with  $x = 1.2$ ). It is a derivative structure of rocksalt  $NiO$ , where Ni vacancies lead to off-stoichiometries ( $x > 1$ ), structural distortions, and p-type conductivity.[49]  $NiO_x$  is selected as a test material because its valence band edge,  $E_{VB,NiO_x}$  is approximately aligned with that of c-Si,  $E_{VB,c-Si}$ , as depicted in **Figure 5(c)** — this was our initial hypothesis of what leads to high performance. Additionally, we expect some tunability of hole doping and  $E_{VB,NiO_x}$  with O/Ni ratio,  $x$ , as explained subsequently. Due to inherent limitations of sputter synthesis and available characterization tools we cannot directly vary all of the six parameters in **Figure 1(a)**, nor can we measure each with certainty, so we limit our extrinsic variables to oxygen ( $O_2$ ) flow rate and thickness  $t$ . These variables should induce changes in intrinsic variables as depicted in **Figure 5(d)**, though we note that varying  $O_2$  flow rate influences multiple material parameters. Namely, we expect  $E_{VB,NiO_x}$  to shift towards vacuum with increased  $x$  and the band gap  $E_G$  to decrease, as elaborated below. Additionally, it has been reported by numerous studies that increasing  $O_2$  during sputter growth reduces resistivity (i.e. increases conductivity) in p-type  $NiO_x$ . [50, 51, 52, 53, 43] Some reports indicate an increase in hole doping and decrease in mobility,[52, 53] but trends and magnitudes are inconsistent.[51, 43] Interfacial defect density  $D_{it}$  is left as a modeled parameter.

1)  $NiO_x$  parameter space: The relations between  $O_2$  flow during synthesis,  $x$  in  $NiO_x$ , and resulting hole doping and  $E_{VB,NiO_x}$  are not reported together in the literature, to our

knowledge. Although widely accepted that  $x > 1$ , the value of  $x$  in  $NiO_x$  is rarely reported, and even more rarely as a function of synthesis conditions. Brückner et al. reports electron probe microanalysis (EPMA) quantification of RF sputtered  $NiO_x$  at varying  $O_2$  gas flows, with synthesis conditions similar to ours but not identical, demonstrating an increase of  $x$  with  $O_2$  flow as shown in **Figure 5(e)** with triangular markers (error bars from EPMA measurement).[46] We roughly estimate that varying  $O_2$  flow in our study from 0 to 9 sccm likely yields an increase of  $x$ , likely somewhere between 1 and 1.4 (blue arrow). We emphasize that parameters such as chamber design and deposition conditions limit the *quantitative* transferability of these literature values, and that  $x$  should be confirmed for our samples by EPMA or another standard-free quantification method. However, what is important here is the *qualitative* demonstration that the increase of  $O_2$  results in the increase of  $x$ , and this qualitative trend has been corroborated by other studies using metallic Ni targets.[41, 42]

In order to assess the role of  $x$  on  $E_{VB,NiO_x}$  and  $E_{G,NiO_x}$ , we obtain the uniform band structure calculations from the Materials Project database of end-points  $NiO$  and  $NiO_2$  ( $x = 1$  and  $x = 2$ , respectively), and calculate their corresponding branch point energy (BPE) values. BPE is a computationally inexpensive metric to qualitatively compare band alignments.[38, 16] In **Figure 5(f)**,  $NiO$  (left) and  $NiO_2$  (right) are aligned to their respective BPE values, denoted by the dashed line, and BPE is estimated for in-between compositions of  $NiO_x$  assuming commensurate structures and Vegard's law with no band bowing. Error bars are calculated using the procedure outlined in Woods-Robinson et al.[16] This suggests that increasing  $x$  from 1 to 2 results in a significantly increased  $E_{VB,NiO_x}$  (by  $\sim 1.25$  eV), a slightly increased  $E_{CB,NiO_x}$  (a value typically held constant in the literature),[30] and slightly decreased  $E_{G,NiO_x}$  as expected from experimental studies.[54] For  $NiO_2$  we plot the experimental layered structure (mp-35925); a structural relationship has been shown in the literature between layered structures and disordered rocksalt structures,[55] supporting this choice of end-point compound, though this trend applies for other  $NiO_2$  polymorphs too (e.g. mp-25428). This relation is merely qualitative; is a notoriously tricky system computationally due to complex defect chemistry and magnetic ordering,[49] and precise alignment calculations are beyond the scope of this study. Furthermore, our  $NiO_x$  films are likely amorphous,[56] and band edges of amorphous semiconductors are not as sharply defined as crystalline materials. However, the key point is that we expect  $x$  to increase and  $E_{VB,NiO_x}$  to shift to lower energy values (closer to vacuum) upon increasing  $O_2$  in the sputter gas. This correlation is supported by Keraudy et al.'s report of an increase of  $E_{VB,NiO_x}$  as  $x$  is increased from 1.01 to 1.14,[54] yet this study uses a metallic Ni target and impulse magnetron sputtering discharge rather than RF sputtering so  $O_2$  flow cannot be directly compared.

2)  $NiO_x$  JV results and simulation fits: **Figure 6(a–e)** reports the JV and performance results of a set of silicon heterojunction (SHJ) solar cells with  $NiO_x$  hole-selective contacts and varying  $O_2$  flow rate (in sccm) during  $NiO_x$  growth. In panel (a) experimental JV curves are reported with solid lines, and the light grey curve corresponds to a standard cell with a (p) a-

**Table II:** Best solar cell results for SHJ cells with NiO<sub>x</sub> hole-selective contacts at various oxygen growth conditions, compared with a standard cell fabricated with a (p) a-Si:H contact.

Flow rate (sccm)	O <sub>2</sub> (%)	η (%)	FF (%)	V <sub>OC</sub> (mV)	J <sub>SC</sub> (mA cm <sup>-2</sup> )	R <sub>S</sub> (Ω cm <sup>2</sup> )
0	0	7.432	59.94	403.6	30.73	2.72
1	0.5	6.807	54.61	410.6	30.36	3.88
5	2.5	4.511	32.91	453.3	30.24	9.53
9	4.5	4.424	28.81	507.9	30.24	11.54
(p) a-Si:H		16.72	78.45	724.4	29.42	2.523

Si:H hole contact. All of the NiO<sub>x</sub> cells have relatively poor V<sub>OC</sub> values, ranging between ~400–500 mV as reported in **Table II** for the four highest-efficiency cells at each condition, and V<sub>OC</sub> increases slightly with O<sub>2</sub> flow. JV curves all have S-shapes, but increasing O<sub>2</sub> flow results in lower FF, lower efficiencies, and more exaggerated S-shapes with a flattening out of the JV curve around the V<sub>OC</sub>. J<sub>SC</sub> values are scattered due to the rudimentary metallization made by shadow masking without influence from O<sub>2</sub> flow. By varying and optimizing O<sub>2</sub> flow and NiO<sub>x</sub> thicknesses, we achieve efficiencies over 7% (O-poor growth conditions) and a maximum V<sub>OC</sub> of just over 500 mV (O-rich growth conditions). This is low compared to standard cells with a (p) a-Si:H hole selective contact, with V<sub>OC</sub> and efficiency of 724.4 mV and 16.72%, respectively, as reported in Table II. However, the trends revealed here and their connection to simulated material parameters still yield important considerations for contact design.

To explore the link between our modeling and experiments, we can fit the NiO<sub>x</sub> JV results from Figure 6 to our AFORS-HET simulations by varying hole doping  $N_A$ ,  $E_{VB,NiO_x}$ , and interfacial defect density  $D_{it}$ . We estimate that  $E_{VB,NiO_x}$  decreases by up to ~0.5 eV with increased O<sub>2</sub> flow ( $E_{VB,NiO_x}$  moves closer to vacuum), as backed out from Figure 5(e) and (f).[46, 54] Hole doping has been reported to widely vary in NiO<sub>x</sub>; for low hole doping densities a VB edge offset of just a few hundred meV should have a significant impact according to our model, but studies have reported hole doping density up to  $\sim 8 \times 10^{19} \text{ cm}^{-3}$  which would give more leniency to  $E_{VB,NiO_x}$ . [52] An example of such fits are plotted with dashed lines in Figure 6(a) for a set of representative JV curves corresponding to O<sub>2</sub> flows of 0, 1, 5, and 9 sccm, with a fixed thickness of 20–25 nm, hole mobility of  $0.1 \text{ cm}^2\text{V}^{-1}\text{s}^{-1}$ , and fit values reported in the figure legend. Fits are performed as well as for a baseline (p) a-Si:H sample, with  $E_{VB,a-Si:H}$  constrained at 5.62 eV,  $N_A = 10^{19} \text{ cm}^{-3}$ , and  $\mu_h = 5 \text{ cm}^2\text{V}^{-1}\text{s}^{-1}$ . A small series resistance of  $0.8 \text{ } \Omega\text{cm}^2$  is added for (p) a-Si:H to improve the fit, and likewise series resistances are added for the NiO<sub>x</sub> cell fits (fitting values are determined by scaling the (p) a-Si:H value according to experimental  $R_S$  values from Table II). Current density is normalized in the simulations to match experimental JV curves, since shadow masking has reduced the J<sub>SC</sub>. We find the simulations to align with experimental results, yielding similar V<sub>OC</sub>, FF and efficiency values as reported with rectangular markers in Figure 6(b–e), as well as closely aligned JV profiles.

Most importantly, this analysis suggests that as  $x$  increases in NiO<sub>x</sub>,  $E_{VB,NiO_x}$  decreases away from the optimum value,

$D_{it}$  decreases, and doping increases. In other words, as O<sub>2</sub> increases, the material is likely less resistive (depending on  $\mu_h$ ), the valence band edge is increasingly misaligned, and the contact is likely better passivated (though still not very passivated). This explains the trade-off between V<sub>OC</sub> and FF in the experimental cells, and the increased S-shape and flattening of JV around V<sub>OC</sub> as O<sub>2</sub> increases. Though useful, we emphasize the reductive nature of fitting; multiple fit values can match experimental data, so we caution quantitative interpretation of these results. Namely, simulated  $E_{VB,NiO_x}$  is somewhat higher than expected from the literature, and the simulated hole doping density for the 0 sccm fit is at the high end for experimental values.[52] Additionally, fit values are only estimates since the simulations ignore intrinsic defects, contact resistances, and other effects. For follow-up work, a measurement of one of the values of  $E_{VB}$  or doping density is important to appropriately constrain the model. We previously measured cells with NiO<sub>x</sub> thicknesses varying from 10–100 nm grown at 0 sccm and 1 sccm.[56] These results demonstrate that performance, namely fill factor, drops very slightly for thicker NiO<sub>x</sub>, also corroborating simulations. Thus, by combining theoretical modeling and real cell measurements, we have demonstrated a link between simulated and experimental performance that can inform searches for a hole-selective contact that is better than NiO<sub>x</sub>.

3) *The role of interfacial defects and non-idealities:* A key takeaway here is that  $D_{it}$  is very high in all NiO<sub>x</sub> cells: non-idealities, likely at the interface, are apparently reducing the performance of these cells. Even the case with the lowest  $D_{it}$  is still over an order of magnitude worse than the  $D_{it}$  modeled in the (p) a-Si:H cell. Nayak et al. have recently achieved higher performing cells with a NiO<sub>x</sub> p-layer,[22] which is probably due to better passivation and lower  $D_{it}$ , but we note this device architecture does *not* use an intrinsic a-Si:H layer so our simulation is not directly transferable here. This corroborates our simulations from Figure 2(a–b). If  $D_{it}$  can be reduced while maintaining the same material parameters, higher efficiencies could be achieved as shown in Figure 3, but only within a very narrow window of parameter space.

The parameter “ $D_{it}$ ” is a cumulative proxy for a wide array of non-idealities that could be occurring in this system as a result of thermodynamic limits, kinetic effects such as sputter damage, and other growth conditions. Defects represented by  $D_{it}$  could induce surface pinning, and could be caused by interfacial layers, phase segregation, and other defects not modeled here including point defects, band edge tail states, extended defects, etc. One likely mechanism leading to non-idealities and high  $D_{it}$  is the chemical instability of the Si / NiO<sub>x</sub> interface and a possible formation of a spurious interfacial layer. To assess whether this may be occurring, we calculate the possible reactions between Si and NiO<sub>x</sub>, assuming thermodynamic equilibrium and 0 K using the Materials Project’s Interfacial Reaction Calculator.[45, 58] We find the following reaction as likely to occur at the interface:



with a reaction enthalpy of -196.8 kJ/mol (-1.224 eV/atom). This finding corroborates literature findings, which report a

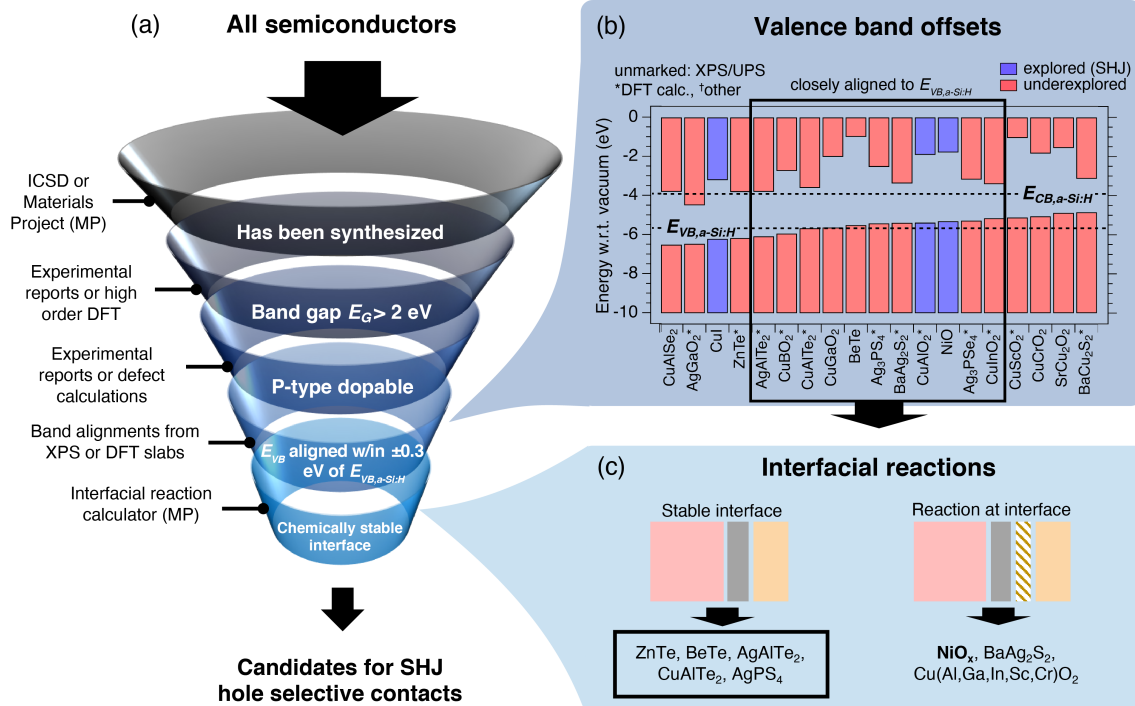


**Figure 7:** (a) “Screening funnel” to search for new candidates as hole-selective contacts in silicon heterojunction solar cells. (b) Band alignment of possible hole-selective contact materials for SHJ solar cells (funnel rung 4), with references for each material’s alignment reported by Woods-Robinson et al.[16, 57] (c) Interfacial reaction calculations of contact materials that resulted from (b), where the extra brown-striped layer indicates an unwanted reaction at the interface (funnel rung 5).

Gibbs free energy change at 1000 K of  $-51.377$  kcal/mol.[59]. Additionally, a thin  $\text{SiO}_x$  is almost certainly forming when the Si wafer is exposed to air. However, charge transport in a thin  $\text{SiO}_x$  layer would likely involve tunnelling through a barrier, and we reiterate that such tunnelling is not included in our simulations and is a limitation of our model. Other possible interfacial reactions could result in the formation of ternary spinel or ilmenite  $\text{Ni}_2\text{SiO}_4$ [60] or metal alloy  $\text{NiSi}_x$ . [61] This formation may cause a trapping layer, leading to increased  $D_{it}$  and other effects. However, as shown recently, it is also possible that  $\text{SiO}_x$  is forming at the interface without a significant detrimental effect on passivation.[62] In fact, Nayak et al. reported that an intentionally introduced  $\text{SiO}_x$  layer actually improves the solar cell performance in (n)c-Si/(i)  $\text{SiO}_x$  / (p)  $\text{NiO}_x$  devices.[22] The implications for an (n)c-Si / (i) a-Si:H / (i)  $\text{SiO}_x$  / (p)  $\text{NiO}_x$  device remain to be explored. Additionally, it remains to be investigated whether spurious phases of Ni metal or  $\text{Ni}_2\text{O}_3$  are present, the role of point defects and extended defects in  $\text{NiO}_x$ , whether hydrogenated  $\text{NiO}_x\text{:H}$  is formed, and whether such hydrogenation or phase segregation could enhance passivation and minimize  $D_{it}$ .

### C. Prospective: exploring new hole-selective contacts in SHJ solar cells

The insights gained from our simulations and the implementation of  $\text{NiO}_x$  as a test material can guide selection of new materials as hole-selective contacts in SHJ solar cells with (i) a-Si:H passivation layers. In particular, we hypothesize that the alignment of the VB edge  $E_{VB}$  of the p-layer to  $E_{VB,a-Si:H}$  is more important than alignment to  $E_{VB,c-Si}$ .

Assuming low  $D_{it}$ , the offset between  $E_{VB}$  and  $E_{VB,a-Si:H}$  should be within approximately  $\pm 0.3$  eV for high doping densities ( $N_A > 10^{18} \text{ cm}^{-3}$ ), with a narrower window when doping is decreased (within  $\pm 0.1$  eV for  $10^{16} \text{ cm}^{-3}$ ). This combination of misaligned  $E_{VB}$  and insufficient doping (as well as defects, thickness, mobility, etc.) might be a reason for the common observation of S-shaped JV curves when integrating novel materials as contacts for SHJ devices. It also is likely why the typical (p) a-Si:H contact performs so well — it is highly dopable, it has a clean interface with (i) a-Si:H, and its VB edge is perfectly aligned to (i) a-Si:H since it is the same material.

Using the criteria outlined in this study, we can define a materials discovery pipeline using a “screening funnel” to search for new hole-selective contacts in SHJ solar cells, depicted in **Figure 7(a)**. A screening funnel is a series of criteria that a material must pass in order to be considered for a certain application.[63] Here, we consider an *ab initio* computational screening procedure using density functional theory (DFT) that can be used by other researchers while searching for new hole-selective contacts. First, it is useful (though not mandatory) to search a space of existing materials. Second, to avoid parasitic absorption, only semi-transparent materials with band gaps greater than approximately 2 eV must be considered (note that this value depends on the DFT functional used; the PBE GGA functional used in the Materials Project database systematically underestimates band gap by 50–100%).[64] We note that the optical absorption coefficient could also be used in this step, but band gap is computationally “cheaper” to calculate so most high-throughput studies use a band gap cutoff as a proxy for absorption edge. Additionally,

we note that this band gap criterion would exclude (p) a-Si:H, as it is not sufficiently transparent. Third, the material should ideally be p-type dopable, though we acknowledge notable exceptions such as  $\text{MoO}_x$ : an alternate contact design approach could use a tunnel or defect recombination junction with an n-type material. P-type doping is trickier to assess computationally,[65] so only experimentally confirmed p-type materials are considered subsequently, but one could use defect calculations to calculate dopability in a screening.[66] Fourth, as discussed above, the VB edge should be aligned to within  $\pm 0.3$  eV of that of a-Si:H, though alignment does not have to be so sharp if doping is high enough. And fifth, as discussed in the previous section, a chemically stable interface with Si is preferable (though not required) to prevent interfacial defects. Other important criteria, such as bond strength and resistance to sputter damage, could be added sequentially after the fifth step. Additionally, the hole-selective material must make good Ohmic contact to a metal (e.g. Ag) in order to transport charge out of the cell, which may not be trivial (we have assumed an ideal Ohmic contact throughout). This is another positive aspect of having high doping in the p-layer, and the choice of metal will depend on band alignment.

In Figure 7(b) and (c), we apply this funnel to a small test set to illustrate its function and to suggest a few candidates for future exploration. Figure 7(b) compares the band offsets for a series of wide band gap p-type materials from the experimental literature (satisfying the first three steps of the funnel), and a box is drawn around the materials with potential promise for SHJ solar cells according to their  $E_{VB}$ . These materials and their offsets are selected from known p-type transparent conductors [16] and from a set of p-type wide band gap chalcogenides.[57] We indicate which of these have been explored in SHJ (purple), as discussed in the Introduction, but many listed materials remain underexplored for device applications (red). Band offsets are from the literature and are derived from both XPS studies and DFT calculations (the latter notated with an asterisk). Perhaps more importantly, understanding of this alignment could lead to a new screening descriptor to inform future computational material discovery studies.

In Figure 7(c), we use the Materials Project’s Interfacial Reaction Calculator to compute reaction energies for the series of materials that emerge from (b).[58] We find that at thermodynamic equilibrium a majority of the compounds boxed in (b), including  $\text{NiO}_x$ , are likely to form a reaction product with Si. In particular, the delafossite materials  $\text{CuMO}_2$  ( $M = \text{Al, Ga, In, Sc, Cr}$ ) are predicted to form a  $\text{SiO}_2$  and other ternary products, while  $\text{BaAg}_2\text{S}_2$  is predicted to form ternary products  $\text{BaAg}_8\text{S}_5$  and  $\text{Ba}_3\text{SiS}_5$ . This formation may or may not be detrimental, as discussed previously, though it adds complication to the device stack and is worth considering. In this example, only p-type telluride compounds such as  $\text{ZnTe}$  and  $\text{AgPS}_4$  emerge from the screening funnel.  $\text{ZnTe}$  is used as the p-type contact in  $\text{CdTe}$  solar cells,[67] and can be alloyed to raise the  $E_{VB}$  closer to vacuum. We note that this calculator is a simple approximation based on convex hull analysis and does not take kinetics into account. Even though they satisfy the funnel criteria, multinary compounds such as  $\text{Ag}_3\text{PS}_4$  may introduce new challenges

into device applications such as detrimental non-equilibrium phase segregation and, if sputter deposited, increased sputter damage. Notably, this test example is only a small subset of possible wide band gap p-type materials. Many computationally predicted p-type transparent conductors (e.g.  $\text{ZrOS}$ ,[18]  $\text{BP}$ ,[17]  $\text{La}_2\text{SeO}_2$ [68]) await experimental investigation and may prove to have appropriate VB edge alignment, dopability, and stability for the hole-selective contact in SHJ applications.

#### IV. CONCLUSION

In SHJ solar cells, a wide band gap p-type hole-selective contact (“p-layer”) with appropriate alignment, doping, and passivation, should reduce parasitic absorption and improve fill factor compared to the standard (p) a-Si:H layer. In this study, we first use simulations to perform a sensitivity analysis of various material parameters for such a p-layer in a simplified device configuration of (n) c-Si / (i) a-Si:H / p-layer. We observe that VB edge energy  $E_{VB}$ , p-type doping,  $D_{it}$ , and thickness are the most important parameters. In particular, we hypothesize that VB edge alignment between the p-layer and (i) a-Si:H is more important than alignment with the (n) c-Si wafer, which is counter to what was previously assumed and could explain the commonly observed S-shaped JV curves for previous attempts to incorporate novel p-type layers as contacts in SHJ cells. We also find that for non-optimal  $E_{VB}$ , increased doping can improve cell performance, in some cases to the same level as for optimal  $E_{VB}$ , so long as  $D_{it}$  is low enough. Our simulation results are supported by experiments using  $\text{NiO}_x$  layers with varying oxygen contents. Namely, we expect that increasing oxygen content should increase VB offset, and show that doing so degrades fill factor and efficiency as expected from the simulations. We hypothesize a very high  $D_{it}$  is responsible for low  $V_{OC}$  values, and reducing detrimental defects is essential for high performance. Based on these findings, we suggest a set of semi-transparent compounds with p-type doping and sufficient VB alignments that merit exploration as hole-selective layers in SHJ solar cells.

This study elicits broader implications for both theorists and engineers in the exploration and development of p-type contacts for device applications, and materials design in general. Device engineers tend to work with a small set of well-investigated conventional semiconductor materials (e.g. Si, GaN, ZnO, ITO);[69] we have discussed strategies for going beyond this paradigm and pairing engineering with new materials discovery. To guide this process, we emphasize the importance of conducting multiparameter analyses to assess how material parameters should be optimized collectively and to determine the ranges of tolerance that enable good device performance. For example, we highlight the tradeoff between high doping and precise band alignment in the SHJ hole selective contact. While searching for new materials, it is also important to consider that a given material does not have fixed properties, but rather allows for a wide range of tunability. Computational screenings, which usually just calculate bulk properties of alloy end-members, ignore such tunability and risk excluding materials on the basis of a false negative, since the end-members do not have the desired property even though the alloy reasonably might.[45] Additionally, tailoring screening criteria to a given application

could prove useful; at least for SHJ applications, achieving a high hole mobility may be less important than other criteria, which counters a general assumption in searches for new p-type transparent conductors that high mobility is a necessity.[18] Ultimately, we demonstrate that a mutually beneficial link between optoelectronic device engineering and computational materials design can be formed: practical material requirements necessary for solving a given device challenge can be used to drive the computational materials design approach while also highlighting new materials for experimental investigation.

#### ACKNOWLEDGMENTS

R. Woods-Robinson acknowledges funding from the NSF GRFP Graduate Fellowship (DGE1106400 and DGE1752814), the U.C. Berkeley Chancellor's Fellowship, and the ThinkSwiss Research Scholarship. The work of A. N. Fioretti was supported by the Horizon 2020 Marie Skłodowska-Curie Actions under Grant 792720 (CLAReTE). K. A. Persson was supported by the U.S. Department of Energy, Office of Science, Office of Basic Energy Sciences, Materials Sciences and Engineering Division under contract no. DE-AC02-05CH11231 (Materials Project program KC23MP). The authors acknowledge funding from the Swiss National Science Foundation under Ambizione Energy grant ICONS (PZENP2173627), technical assistance from Paratte Vincent Philippe and Sylvain Dunand, and fruitful discussion with Antognini Luca Massimiliano, Dr. Sihua Zhong, Dr. Shyam Dwaraknath, and Dr. Matthew K. Horton.

#### AUTHOR CONTRIBUTIONS

Conceptualization, A.F., R.W.R., and M.B.; Methodology, R.W.R. and A.F.; Investigation, R.W.R., A.F., M.B.; Writing, R.W.R.; Funding Acquisition, R.W.R., A.F., M.B., C.B.; Supervision, A.F., J.H., M.B., K.A.P., C.B.

#### REFERENCES

- [1] K. Yoshikawa, H. Kawasaki, W. Yoshida, T. Irie, K. Konishi, K. Nakano, T. Uto, D. Adachi, M. Kanematsu, H. Uzu *et al.*, "Silicon heterojunction solar cell with interdigitated back contacts for a photoconversion efficiency over 26%," *Nature Energy*, vol. 2, no. 5, p. 17032, 2017.
- [2] J. Haschke, O. Dupré, M. Boccard, and C. Ballif, "Silicon heterojunction solar cells: Recent technological development and practical aspects-from lab to industry," *Solar Energy Materials and Solar Cells*, vol. 187, pp. 140–153, 2018.
- [3] A. Onno, C. Chen, P. Koswatta, M. Boccard, and Z. C. Holman, "Passivation, conductivity, and selectivity in solar cell contacts: Concepts and simulations based on a unified partial-resistances framework," *Journal of Applied Physics*, vol. 126, no. 18, p. 183103, 2019.
- [4] J. Bullock, A. Cuevas, T. Allen, and C. Battaglia, "Molybdenum oxide moox: A versatile hole contact for silicon solar cells," *Applied Physics Letters*, vol. 105, no. 23, p. 232109, 2014.
- [5] J. Geissbühler, J. Werner, S. Martin de Nicolas, L. Barraud, A. Hessler-Wyser, M. Despeisse, S. Nicolay, A. Tomasi, B. Niesen, S. De Wolf *et al.*, "22.5% efficient silicon heterojunction solar cell with molybdenum oxide hole collector," *Applied Physics Letters*, vol. 107, no. 8, p. 081601, 2015.
- [6] J. Dréon, Q. Jeangros, J. Cattin, J. Haschke, L. Antognini, C. Ballif, and M. Boccard, "23.5%-efficient silicon heterojunction silicon solar cell using molybdenum oxide as hole-selective contact," *Nano Energy*, vol. 70, p. 104495, 2020.
- [7] L. Mazzarella, S. Kirner, B. Stannowski, L. Korte, B. Rech, and R. Schlattmann, "p-type microcrystalline silicon oxide emitter for silicon heterojunction solar cells allowing current densities above 40 ma/cm<sup>2</sup>," *Applied Physics Letters*, vol. 106, no. 2, p. 023902, 2015.
- [8] A. N. Fioretti, M. Boccard, R. Monnard, and C. Ballif, "Low-temperature p-type microcrystalline silicon as carrier selective contact for silicon heterojunction solar cells," *IEEE Journal of Photovoltaics*, vol. 9, no. 5, pp. 1158–1165, 2019.
- [9] A. E. Delahoy and S. Guo, "Transparent conducting oxides for photovoltaics," *Handbook of Photovoltaic Science and Engineering*, pp. 716–796, 2011.
- [10] A. Banerjee and K. Chattopadhyay, "Recent developments in the emerging field of crystalline p-type transparent conducting oxide thin films," *Progress in Crystal Growth and Characterization of materials*, vol. 50, no. 1-3, pp. 52–105, 2005.
- [11] A. N. Fioretti and M. Morales-Masis, "Bridging the p-type transparent conductive materials gap: synthesis approaches for disperse valence band materials," *Journal of Photonics for Energy*, vol. 10, no. 4, p. 042002, 2020.
- [12] A. Walsh and J.-S. Park, "The holey grail of transparent electronics," *Matter*, vol. 3, no. 3, pp. 604–606, 2020.
- [13] S. Liu, R. Liu, Y. Chen, S. Ho, J. H. Kim, and F. So, "Nickel oxide hole injection/transport layers for efficient solution-processed organic light-emitting diodes," *Chemistry of Materials*, vol. 26, no. 15, pp. 4528–4534, 2014.
- [14] S. A. Makhlof, "Electrical properties of nio films obtained by high-temperature oxidation of nickel," *Thin Solid Films*, vol. 516, no. 10, pp. 3112–3116, 2008.
- [15] H. Wu and L.-S. Wang, "A study of nickel monoxide (nio), nickel dioxide (onio), and ni (o 2) complex by anion photoelectron spectroscopy," *The Journal of chemical physics*, vol. 107, no. 1, pp. 16–21, 1997.
- [16] R. Woods-Robinson, D. Broberg, A. Faghaninia, A. Jain, S. S. Dwaraknath, and K. A. Persson, "Assessing high-throughput descriptors for prediction of transparent conductors," *Chemistry of Materials*, vol. 30, no. 22, pp. 8375–8389, 2018.
- [17] J. B. Varley, A. Miglio, V.-A. Ha, M. J. van Setten, G.-M. Rignanese, and G. Hautier, "High-throughput design of non-oxide p-type transparent conducting materials: Data mining, search strategy, and identification of boron phosphide," *Chemistry of Materials*, vol. 29, no. 6, pp. 2568–2573, 2017.
- [18] G. Hautier, A. Miglio, G. Ceder, G.-M. Rignanese, and X. Gonze, "Identification and design principles of low hole effective mass p-type transparent conducting oxides," *Nature communications*, vol. 4, p. 2292, 2013.
- [19] G. Brunin, F. Ricci, V.-A. Ha, G.-M. Rignanese, and G. Hautier, "Transparent conducting materials discovery using high-throughput computing," *npj Computational Materials*, vol. 5, no. 1, p. 1, 2019.
- [20] T. Arai, S. Iimura, J. Kim, Y. Toda, S. Ueda, and H. Hosono, "Chemical design and example of transparent bipolar semiconductors," *Journal of the American Chemical Society*, vol. 139, no. 47, pp. 17175–17180, 2017.
- [21] F. Menchini, M. L. Grilli, T. Dikonimos, A. Mittiga, L. Serenelli, E. Salza, R. Chierchia, and M. Tucci, "Application of niox thin films as p-type emitter layer in heterojunction solar cells," *physica status solidi (c)*, vol. 13, no. 10-12, pp. 1006–1010, 2016.
- [22] M. Nayak, S. Mandal, A. Pandey, S. Mudgal, S. Singh, and V. K. Komarala, "Nickel oxide hole-selective heterocontact for silicon solar cells: Role of siox interlayer on device performance," *Solar RRL*, vol. 3, no. 11, p. 1900261, 2019.
- [23] R. Stangl, M. Kriegl, and M. Schmidt, "Aforshet, version 2.2, a numerical computer program for simulation of heterojunction solar cells and measurements," in *2006 IEEE 4th World Conference on Photovoltaic Energy Conference*, vol. 2. IEEE, 2006, pp. 1350–1353.
- [24] R. Varache, C. Leendertz, M. Gueunier-Farret, J. Haschke, D. Muñoz, and L. Korte, "Investigation of selective junctions using a newly developed tunnel current model for solar cell applications," *Solar Energy Materials and Solar Cells*, vol. 141, pp. 14–23, 2015.
- [25] M. Schmidt, L. Korte, A. Laades, R. Stangl, C. Schubert, H. Angermann, E. Conrad, and K. Maydell, "Physical aspects of a-si: H/c-si heterojunction solar cells," *Thin Solid Films*, vol. 515, no. 19, pp. 7475–7480, 2007.
- [26] J.-P. Kleider, A. Gudovskikh, and P. Roca i Cabarrocas, "Determination of the conduction band offset between hydrogenated amorphous silicon and crystalline silicon from surface inversion layer conductance measurements," *Applied Physics Letters*, vol. 92, no. 16, p. 162101, 2008.
- [27] O. Madelung, *Semiconductors: data handbook*. Springer Science & Business Media, 2012.
- [28] R. Varache, J.-P. Kleider, M.-E. Gueunier-Farret, and L. Korte, "Silicon heterojunction solar cells: Optimization of emitter and contact properties from analytical calculation and numerical simulation," *Materials Science and Engineering: B*, vol. 178, no. 9, pp. 593–598, 2013.
- [29] J. Wang, F. Meng, Z. Fang, and Q. Ye, "Investigation of a-si (n+)/c-si (p) hetero-junction solar cell through aforshet simulation," *Surface and Interface Analysis*, vol. 43, no. 9, pp. 1211–1217, 2011.

- [30] H. Imran, T. M. Abdolkader, and N. Z. Butt, "Carrier-selective nio/si and tio 2/si contacts for silicon heterojunction solar cells," *IEEE Transactions on Electron Devices*, vol. 63, no. 9, pp. 3584–3590, 2016.
- [31] S. Nakano and Y. Takeuchi, "Experimental and simulation studies of interface properties of crystalline germanium heterojunction solar cells," in *2014 IEEE International Nanoelectronics Conference (INEC)*. IEEE, 2014, pp. 1–5.
- [32] P. E. Blöchl, "Projector augmented-wave method," *Phys. Rev. B*, vol. 50, no. 24, p. 17953, 1994.
- [33] G. Kresse and D. Joubert, "From ultrasoft pseudopotentials to the projector augmented-wave method," *Phys. Rev. B*, vol. 59, no. 3, pp. 1758–1775, 1999.
- [34] G. Kresse and J. Hafner, "Ab initio molecular dynamics for liquid metals," *Phys. Rev. B*, vol. 47, no. 1, pp. 558–561, 1993.
- [35] G. Kresse and J. Furthmüller, "Efficient iterative schemes for ab initio total-energy calculations using a plane-wave basis set," *Phys. Rev. B*, vol. 54, no. 16, p. 11169, 1996.
- [36] J. P. Perdew, K. Burke, and M. Ernzerhof, "Generalized gradient approximation made simple," *Phys. Rev. Letters*, vol. 77, no. 18, p. 3865, 1996.
- [37] A. Jain, G. Hautier, S. P. Ong, C. J. Moore, C. C. Fischer, K. A. Persson, and G. Ceder, "Formation enthalpies by mixing gga and gga+ u calculations," *Physical Review B*, vol. 84, no. 4, p. 045115, 2011.
- [38] A. Schleife, F. Fuchs, C. Rödl, J. Furthmüller, and F. Bechstedt, "Branch-point energies and band discontinuities of iii-nitrides and iii-ii-oxides from quasiparticle band-structure calculations," *Applied Physics Letters*, vol. 94, no. 1, p. 012104, 2009.
- [39] L. Ward, A. Dunn, A. Faghaninia, N. E. Zimmermann, S. Bajaj, Q. Wang, J. Montoya, J. Chen, K. Bystrom, M. Dylla *et al.*, "Matminer: An open source toolkit for materials data mining," *Computational Materials Science*, vol. 152, pp. 60–69, 2018.
- [40] R. Stangl, C. Leendertz, and J. Haschke, "Numerical simulation of solar cells and solar cell characterization methods: the open-source on demand program afors-het," *Solar Energy*, vol. 14, pp. 319–352, 2010.
- [41] Y.-M. Lu, W.-S. Hwang, J. Yang, and H. Chuang, "Properties of nickel oxide thin films deposited by rf reactive magnetron sputtering," *Thin Solid Films*, vol. 420, pp. 54–61, 2002.
- [42] I. Hotový, J. Huran, J. Janik, and A. Kobzev, "Deposition and properties of nickel oxide films produced by dc reactive magnetron sputtering," *Vacuum*, vol. 51, no. 2, pp. 157–160, 1998.
- [43] P. Salunkhe, M. A. AV, and D. Kekuda, "Investigation on tailoring physical properties of nickel oxide thin films grown by dc magnetron sputtering," *Materials Research Express*, vol. 7, no. 1, p. 016427, 2020.
- [44] M. A. Leilaouioun, W. Weigand, M. Boccard, J. Y. Zhengshan, K. Fisher, and Z. C. Holman, "Contact resistivity of the p-type amorphous silicon hole contact in silicon heterojunction solar cells," *IEEE Journal of Photovoltaics*, vol. 10, no. 1, pp. 54–62, 2019.
- [45] A. Jain, S. P. Ong, G. Hautier, W. Chen, W. D. Richards, S. Dacek, S. Cholia, D. Gunter, D. Skinner, G. Ceder *et al.*, "Commentary: The materials project: A materials genome approach to accelerating materials innovation," *Apl Materials*, vol. 1, no. 1, p. 011002, 2013.
- [46] W. Brückner, R. Kaltofen, J. Thomas, M. Hecker, M. Uhlemann, S. Oswald, D. Elefant, and C. Schneider, "Stress development in sputtered nio thin films during heat treatment," *Journal of applied physics*, vol. 94, no. 8, pp. 4853–4858, 2003.
- [47] U. Rau and T. Kirchartz, "Charge carrier collection and contact selectivity in solar cells," *Advanced Materials Interfaces*, vol. 6, no. 20, p. 1900252, 2019.
- [48] P. Procel, G. Yang, O. Isabella, and M. Zeman, "Theoretical evaluation of contact stack for high efficiency ibc-shj solar cells," *Solar Energy Materials and Solar Cells*, vol. 186, pp. 66–77, 2018.
- [49] W.-B. Zhang, N. Yu, W.-Y. Yu, and B.-Y. Tang, "Stability and magnetism of vacancy in nio: a gga+ u study," *The European Physical Journal B*, vol. 64, no. 2, pp. 153–158, 2008.
- [50] M. Grilli, F. Menchini, T. Dikonimos, P. Nunziante, L. Pilloni, M. Yilmaz, A. Piegari, and A. Mittiga, "Effect of growth parameters on the properties of rf-sputtered highly conductive and transparent p-type niox films," *Semiconductor Science and Technology*, vol. 31, no. 5, p. 055016, 2016.
- [51] J. Kim, Y. Ko, and K. Park, "Effect of rf magnetron sputtered nickel oxide thin films as an anode buffer layer in a p 3 ht: Pcbm bulk hetero-junction solar cells," *Acta Physica Polonica, A.*, vol. 133, no. 4, 2018.
- [52] H. Sun, S.-C. Chen, W.-C. Peng, C.-K. Wen, X. Wang, and T.-H. Chuang, "The influence of oxygen flow ratio on the optoelectronic properties of p-type ni1-xo films deposited by ion beam assisted sputtering," *Coatings*, vol. 8, no. 5, p. 168, 2018.
- [53] M. I. Pintor-Monroy, B. L. Murillo-Borjas, M. Catalano, and M. A. Quevedo-Lopez, "Controlling carrier type and concentration in nio films to enable in situ pn homojunctions," *ACS applied materials & interfaces*, vol. 11, no. 30, pp. 27 048–27 056, 2019.
- [54] J. Keraudy, B. Delfour-Peyrethron, A. Ferrec, J. Garcia Molleja, M. Richard-Plouet, C. Payen, J. Hamon, B. Corraze, A. Goullet, and P.-Y. Jouan, "Process-and optoelectronic-control of niox thin films deposited by reactive high power impulse magnetron sputtering," *Journal of Applied Physics*, vol. 121, no. 17, p. 171916, 2017.
- [55] J. Lee, A. Urban, X. Li, D. Su, G. Hautier, and G. Ceder, "Unlocking the potential of cation-disordered oxides for rechargeable lithium batteries," *science*, vol. 343, no. 6170, pp. 519–522, 2014.
- [56] R. Woods-Robinson, A. Fioretti, J. Haschke, K. Persson, M. Boccard, and C. Ballif, "Linking simulation and synthesis of nickel oxide hole-selective contacts for silicon heterojunction solar cells," in *2020 IEEE 47nd Photovoltaic Specialist Conference (PVSC)*. IEEE, 2020, pp. 1–5.
- [57] R. Woods-Robinson, Y. Han, H. Zhang, T. Ablekim, I. Khan, K. A. Persson, and A. Zakutayev, "Wide band gap chalcogenide semiconductors," *Chemical Reviews*, 2020.
- [58] W. D. Richards, L. J. Miara, Y. Wang, J. C. Kim, and G. Ceder, "Interface stability in solid-state batteries," *Chemistry of Materials*, vol. 28, no. 1, pp. 266–273, 2015.
- [59] K. Hubbard and D. Schlom, "Thermodynamic stability of binary oxides in contact with silicon," *Journal of Materials Research*, vol. 11, no. 11, pp. 2757–2776, 1996.
- [60] A. Ringwood, "Prediction and confirmation of olivine—spinel transition in ni2sio4," *Geochimica et Cosmochimica Acta*, vol. 26, no. 4, pp. 457–469, 1962.
- [61] R. Thompson, J. Angilello, and K.-N. Tu, "Crystallization kinetics of amorphous nix films," *Thin solid films*, vol. 188, no. 2, pp. 259–265, 1990.
- [62] S. Zhong, J. Dreon, Q. Jeangros, E. Aydin, S. De Wolf, F. Fu, M. Boccard, and C. Ballif, "Mitigating plasmonic absorption losses at rear electrodes in high-efficiency silicon solar cells using dopant-free contact stacks," *Advanced Functional Materials*, vol. 30, no. 5, p. 1907840, 2020.
- [63] G. Hautier, "Finding the needle in the haystack: Materials discovery and design through computational ab initio high-throughput screening," *Computational Materials Science*, vol. 163, pp. 108–116, 2019.
- [64] M. Chan and G. Ceder, "Efficient band gap prediction for solids," *Physical review letters*, vol. 105, no. 19, p. 196403, 2010.
- [65] A. Goyal, P. Gorai, S. Anand, E. S. Toberer, G. J. Snyder, and V. Stvanović, "On the dopability of semiconductors and governing materials properties," *Chemistry of Materials*, 2020.
- [66] D. Broberg, B. Medasani, N. E. Zimmermann, G. Yu, A. Canning, M. Haranczyk, M. Asta, and G. Hautier, "Pycdt: A python toolkit for modeling point defects in semiconductors and insulators," *Comput. Phys. Commun.*, vol. 226, pp. 165 – 179, 2018. [Online]. Available: <http://www.sciencedirect.com/science/article/pii/S0010465518300079>
- [67] C. A. Wolden, A. Abbas, J. Li, D. R. Diercks, D. M. Meysing, T. R. Ohno, J. D. Beach, T. M. Barnes, and J. M. Walls, "The roles of znte buffer layers on cdte solar cell performance," *Solar energy materials and solar cells*, vol. 147, pp. 203–210, 2016.
- [68] N. Sarmadian, R. Saniz, B. Partoens, and D. Lamoen, "Easily doped p-type, low hole effective mass, transparent oxides," *Scientific reports*, vol. 6, p. 20446, 2016.
- [69] M. E. Levinshtein, S. L. Rumyantsev, and M. S. Shur, *Properties of Advanced Semiconductor Materials: GaN, AlN, InN, BN, SiC, SiGe*. John Wiley & Sons, 2001.